

Oxygenation of CO and NO on Amorphous Solid Water

Meenu Upadhyay and Markus Meuwly*

*Department of Chemistry, University of Basel, Klingelbergstrasse 80, CH-4056 Basel,
Switzerland.*

E-mail: m.meuwly@unibas.ch

March 25, 2024

Abstract

Context. The dynamics for molecule formation, relaxation, diffusion, and desorption on amorphous solid water is studied in a quantitative fashion.

Aims. We aim at characterizing, at a quantitative level, the formation probability, stabilization, energy relaxation and diffusion dynamics of CO₂ and NO₂ on cold amorphous solid water following atom+diatom recombination reactions.

Methods. Accurate machine-learned energy functions combined with fluctuating charge models were used to investigate the diffusion, interactions, and recombination dynamics of atomic oxygen with CO and NO on amorphous solid water (ASW). Energy relaxation to the ASW and into water-internal-degrees of freedom were determined from analysis of the vibrational density of states. The surface diffusion and desorption energetics was investigated from extended and nonequilibrium MD simulations.

Results. The reaction probability on the nanosecond time scale is determined in a quantitative fashion and demonstrates that surface diffusion of the reactants leads to recombination for initial separations up to 20 Å. After recombination both, CO₂ and

NO₂, stabilize by energy transfer to water internal and surface phonon modes on the picosecond time scale. The average diffusion barriers and desorption energies agree with those reported from experiments. After recombination, the triatomic products diffuse easily which contrasts with the equilibrium situation in which both, CO₂ and NO₂, are stationary on the multi-nanosecond time scale.

1 Introduction

Surface processes are of paramount importance for the genesis of molecules in the universe. In the interstellar medium, nitrogen emerges as one of the chemically dynamic species, following hydrogen, oxygen, and carbon. Within the realm of prebiotic molecules and simple amino acids including CH₂NH, CH₃NH₂, NH₂CH₂COOH, NH₂CHO, HNCO, nitrogen stands out as the common element, underscoring the necessity of exploring the reactivity of nitrogen-containing molecules. This is because three-body collisions in the gas phase are highly inefficient for molecule formation from atomic constituents. Astrophysically relevant surfaces consist of silicates, carbonaceous species (graphite, amorphous carbon, polycyclic aromatic hydrocarbons), or water.¹ In cold molecular clouds, cosmic dust grains are typically covered by water ice which can be polycrystalline or amorphous (ASW). At low temperatures, ASW dominates over the polycrystalline phase.² Typically, bulk water is present in the form of ASW which is the main component of interstellar ices.³ The structure of ASW is usually probed by spectroscopic measurements^{3,4} although interference-based methods have also been employed.⁵ ASWs are porous structures characterized by surface roughness and internal cavities of different sizes which can retain molecular or atomic guests.⁶ Under laboratory conditions the water ices have been reported to be porous^{7,8} or non-porous⁷⁻⁹ ASW whereas the morphology of ices in the interstellar medium is more heavily debated.^{10,11}

The high porosity of ASW¹²⁻¹⁴ makes it a suitable catalyst for gas-surface reactions involving oxygen,¹⁵⁻²² hydrogen,²³ carbonaceous²⁴⁻²⁷ and nitrogen-containing²⁸ species. The surface

morphology and chemistry help to adsorb chemical reagents on top of²⁹ or inside ASW.^{30,31} This increases the probability for the reaction partners to diffuse to locations for collisions and association reactions to occur. As the diffusivity of individual atoms and small molecules has been established from both, experiments and simulations,^{20,24,32} this is a likely scenario for formation of molecules on and within ASW.

The chemical precursors for formation of CO₂ are believed to be carbon monoxide and atomic oxygen and the CO+O reaction has been proposed as a non-energetic pathway, close to conditions in interstellar environments, for CO₂ formation 20 years ago from experiments involving a water-ice cap on top of CO and O deposited on a copper surface.³³ Formation of CO₂(¹Σ_g⁺) from ground state CO(¹Σ⁺) and electronically excited O(¹D) is barrierless. In addition to CO₂, nitrogen-containing species, such as nitric oxide (NO),^{34–38} nitrous oxide (N₂O)^{35,39} and nitrosyl hydride (HNO)⁴⁰ have been detected in the interstellar medium. However, their interstellar chemistry has been little explored so far. Specifically, NO is believed to be critical for the overall nitrogen chemistry of the interstellar medium.^{41,42}

The quest of the present work is to investigate the energetics and dynamics of the CO and NO oxygenation reactions O(¹D)+CO(¹Σ⁺) and O(³P) + NO(X²Π) on ASW to form ground state CO₂(¹Σ_g⁺) and NO₂(²A'), respectively, at conditions representative of interstellar environments. Electronically excited atomic oxygen species can, for example, be generated from photolysis of H₂O⁴³ which has a radiative lifetime of 110 minutes.⁴⁴ An alternative pathway proceeds via electron-induced neutral dissociation of water into H₂ + O(¹D).⁴⁵ In the presence of CO, formation of CO₂ in cryogenic CO/H₂O films was observed.⁴⁵ Ground state ³P atomic oxygen was observed from photolysis of O₂ using far-ultraviolet light.⁴⁶ These are also formation routes of O(³P / ¹D) that can occur in interstellar photon dominated regions.

The present work first describes the methods used. This is followed by CO₂ and NO₂ for-

mation dynamics in their electronic ground states. Next, desorption dynamics of the species involved is considered and energy redistribution is analyzed. Finally, conclusions are drawn.

2 Methods

2.1 Intermolecular Interactions

Reactive molecular dynamics simulations require potential energy surfaces (PESs) that allow bond formation and bond breaking.⁴⁷ Two such PESs were considered in the present work. One was based on fitting Morse potentials $V(r) = D_e(1 - \exp\{-\beta(r - r_0)^2\})$ to the N/C–O interaction based on *ab initio* calculations using the MOLPRO⁴⁸ suite of programs at the MRCI/aug-cc-pVTZ level of theory.^{49,50} The bending force constants were adapted to match with experimental frequencies. The bending frequency for CO₂ and NO₂ are at 660 cm⁻¹ and 750 cm⁻¹ respectively which compares with 667 cm⁻¹ and 750 cm⁻¹ from experiments. For the angular potential (the OCO/ONO bend), the parameters were those from the CHARMM36 force field⁵¹ and this PES is referred to as MMH (for Morse-Morse-Harmonic). Such an approach is similar to that used previously for oxygen-oxygen recombination on amorphous solid water.^{21,52} The second set of PESs were reproducing kernel Hilbert Space (RKHS) representations of reference energies computed using MOLPRO.⁴⁸ For CO₂ and NO₂, CCSD(T)-F12/aug-cc-pVTZ-F12⁵³ and MRCI+Q/aug-cc-pVTZ⁵⁴ level ground state PESs were used to run the dynamics.

At the low temperatures prevalent in the interstellar medium diffusion is a major driving force for chemical reactions. To provide an accurate depiction of this phenomena, the fluctuating point charge (FPC) model is used for CO, NO and atomic oxygen. In such a model the point charges of CO, NO and atomic oxygen fluctuate as a function of the OC/ON–O separation, see Figure S1. Mulliken charges were obtained from DFT (M062x/aug-cc-pvtz)

calculations of snapshots from the MD simulations with OC/NO—O adsorbed on a cluster containing the 10 nearest H₂O molecules with standard van der Waals parameters from CHARMM36 force field.⁵¹ After inspection of the charge variations depending on geometry, a sigmoidal function parametrization $y = a + \frac{b-a}{1+e^{\frac{c-r}{d}}}$ was used to determine charges as a function of r , where r is the distance between “C/N” of OC/ON diatomics and atomic oxygen. For distances $r > 3.0$ Å the diatomics and atomic oxygen behave as neutrals on the water surfaces which significantly affects their diffusion behaviour.

2.2 Molecular Dynamics Simulations

All molecular dynamics (MD) simulations were carried out using the CHARMM suite of programs⁵⁵ with provisions for bond forming reactions through MMH or RKHS representations,⁵⁶ see above. The simulation system, see Figure 1, consisted of an equilibrated cubic box of amorphous solid water containing 1000 water molecules with dimension $31 \times 31 \times 31$ Å³. Simulations were started from an existing, equilibrated ASW structure^{20,21,53} by adding adsorbates (CO, NO, O) on top of ASW.

In the following, the coordinates are the diatomic stretch r , the separation R between the center of mass of the diatom and the oxygen atom, and θ is the angle between \vec{R} and \vec{r} . Initial conditions (coordinates and velocities) were generated for a grid of angles θ and separations R . With CO/NO and O constrained at given values of R and θ , first 750 steps of steepest descent and 100 steps Adopted Basis Newton-Raphson minimization were carried out. This was followed by 50 ps of heating dynamics to 50 K. Then, 100 ps equilibration with R and θ still constrained dynamics simulations were carried out at 50 K. From each of the runs coordinates and velocities were saved regularly to obtain initial conditions for each combination of angle and distance. Production simulations 500 ps in length were then run from saved coordinates and velocities in the NVE ensemble. Data (energies, coordinates

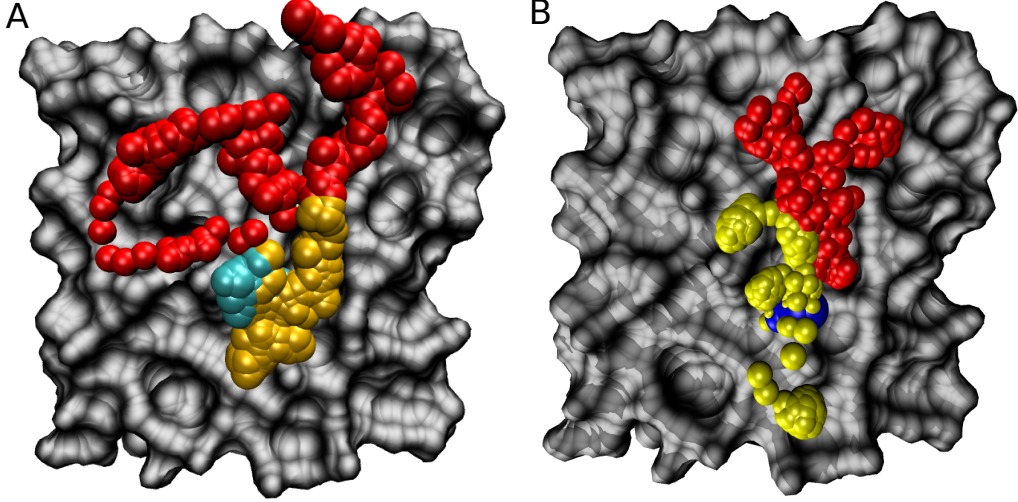


Figure 1: The simulation system for studying the CO_2 (Panel A) and NO_2 (Panel B) recombination reaction. Panel A color code: oxygen (red), CO (cyan), CO_2 (orange); Panel B color code: oxygen (red), NO (blue), NO_2 (yellow). Before and after recombination all species diffuse on the water surface in this case.

and velocities) were saved every 0.5 ps for subsequent analysis.

2.3 Analysis

To characterize energy flow between the activated internal modes of newly formed species and the surface water molecules, the vibrational density of states (vDOS) was analyzed.^{57,58} For this, the Fourier transform of the hydrogen atoms normalized velocity autocorrelation function was determined⁵⁹ according to

$$I_{\text{vDOS}}(\omega) = \int_0^{T_c} \frac{\langle v(0) \cdot v(t) \rangle}{\langle v(0) \cdot v(0) \rangle} e^{-i2\pi\omega t} dt \quad (1)$$

where v denotes the velocity vector of the hydrogen atom and $T_c = 1$ ps.

3 Results

3.1 Exploratory Simulations

A representative 500 ps trajectory for $\text{CO}_A + \text{O}_B$ recombination is shown in Figure 2 (left column). Initially, the $\text{C} \cdots \text{O}_B$ separation is $\sim 12 \text{ \AA}$ (see panel A). For the first 190 ps, oxygen diffusion on the water surface can be seen. Upon recombination at $t \sim 190 \text{ ps}$ the CO stretch and the OCO (panel B) angle are highly excited and relax during the following few picoseconds to average values around the CO_2 equilibrium geometry. The CO_2 product remains in an internally excited state for a considerably longer time scale, see panel B. The temperatures of the ASW (cyan) and the full system (black) are determined by the kinetic energies of the molecules. A prominent peak in the temperature of full system is observed right after recombination whereas the warming of cool water surface is gradual (panel C inset).

Figure 2 (right column) shows a $\text{NO}_A + \text{O}_B$ recombination trajectory. The ground state $\text{NO}_2(^2A')$ has a nonlinear geometry with N-O distances of 1.2 \AA and O-N-O angle of 134° . In this case, recombination takes place after $\sim 110 \text{ ps}$ and the amount of energy released is half compared to the CO_2 . This is due to the different stabilization energies of the triatomics with respect to the $\text{CO/NO}+\text{O}$ asymptote which are 7.71 eV for CO_2 (for $\theta = 180^\circ$) and 3.24 eV for NO_2 (for $\theta = 135^\circ$), respectively.

3.2 Reaction Probabilities for CO_2 and NO_2 Formation

The formation dynamics of CO_2 and NO_2 was followed from initial conditions on a (R, θ) grid. For each initial R and θ configuration, 250 or 500 trajectories at 50 K were run for 500 ps. Depending on the initial (R, θ) values heat maps of the formation probability were determined and a kernel density estimate (KDE) was used for smoothing, see Figures 3 and 4.

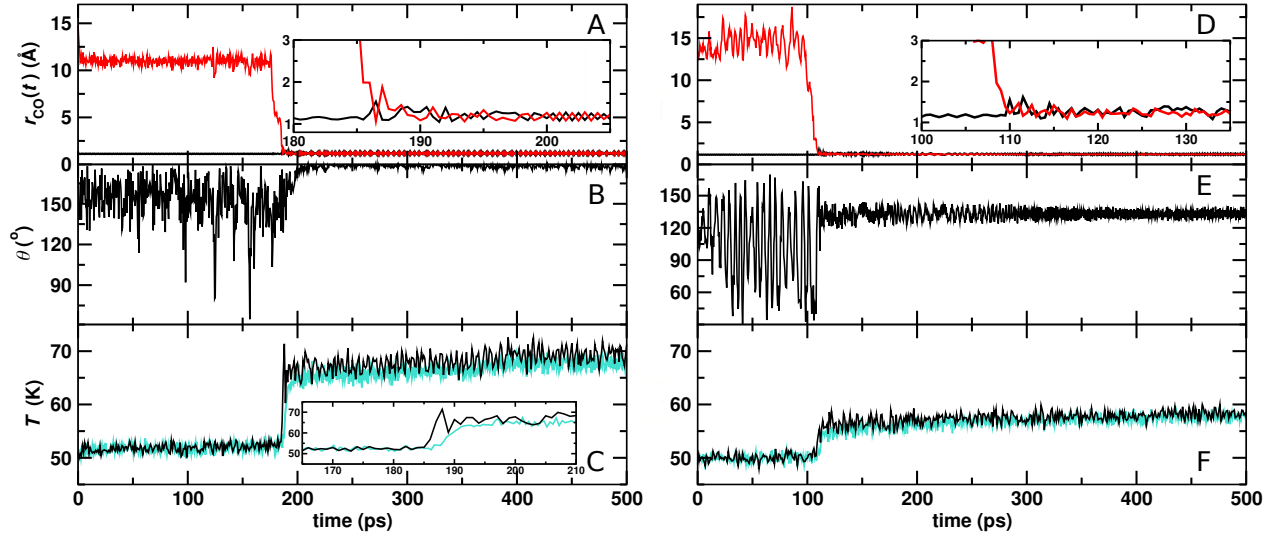


Figure 2: Recombination of $\text{CO} + \text{O}$ to form CO_2 (left column) and $\text{NO} + \text{O}$ to NO_2 (right column) in ground state. Panel A and D: $\text{O}_B\text{-C/N}$ (red) and $\text{O}_A\text{-C/N}$ (black) separation; Panel B and E: O-C/N-O angle; Panel C and F: Temperature of the ASW (cyan) and the full system (black) before and after recombination. Upon recombination both O-C/N stretches exhibit equally pronounced excitation (shown in the insets).

Figure 3 reports probability heat maps for the likelihood to form CO_2 depending on initial (R, θ) using both MMH (Panel A) and RKHS (Panel B) PESs from simulations 500 ps in length. With the MMH PES (Panel A) for $R \sim 2$ to 4.5 the recombination probability is $P \sim 1$ near 180° and vanishes for $\theta \sim 90^\circ$. For $\theta = 180^\circ$, P changes from unity for $R = 4$ to $P \sim 0$ for 14 \AA on the 500 ps time scale. For $R > 4 \text{ \AA}$ and $\theta \leq 120^\circ$ the formation probability is $P = 0$.

Using the RKHS PES, which is a considerably more accurate representation of the $\text{O}+\text{CO}$ interaction than the MMH parametrization, the reaction probabilities depending on initial (R, θ) is larger throughout, see Figure 3 B. In particular along the angular coordinate θ the probability for formation of CO_2 is increased. These differences are due to the different

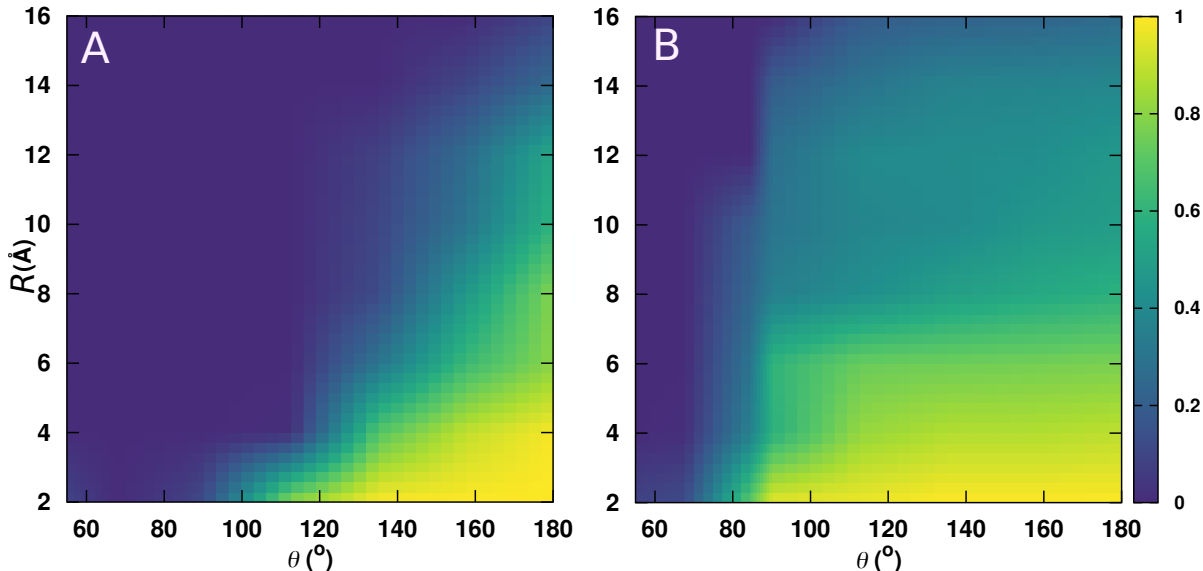


Figure 3: KDE density map for the average CO_2 formation probability depending on initial (R, θ) using the MMH (Panel A) and RKHS (Panel B) PES. The color palette indicates the probability of the reaction, with yellow representing $P = 1$ and blue representing $P = 0$. The COO formation probability using RKHS PES is shown in Figure S2.

topographies of the two PESs. Also, the angular dependence is observed for $R < 7 \text{\AA}$ and for larger distances $R > 7 \text{\AA}$ a plateau is observed. This plateau implies that the reaction probability is primarily governed by diffusion for large distances and does not depend on the initial angular term on the 500 ps time scale.

Due to the more realistic and improved charge model for the reactants, their diffusivity increases. For simulations on the 500 ps this leads to a nonvanishing reaction probability for initial separations of $R = 16 \text{\AA}$. This contrasts remarkably with earlier simulations Upadhyay et al.⁵³ that maintained the charges on the oxygen atom and CO molecule fixed at $\pm 0.3e$ (corresponding to their charges in CO_2) which suppressed the reactants' mobility and reaction probability for $R > 5 \text{\AA}$ for simulations on the same time scale. Overall, using the more realistic charge models from the present work increases the recombination probability of the species involved.

The recombination probability for NO_2 formation is reported in Figure 4. Panel A shows

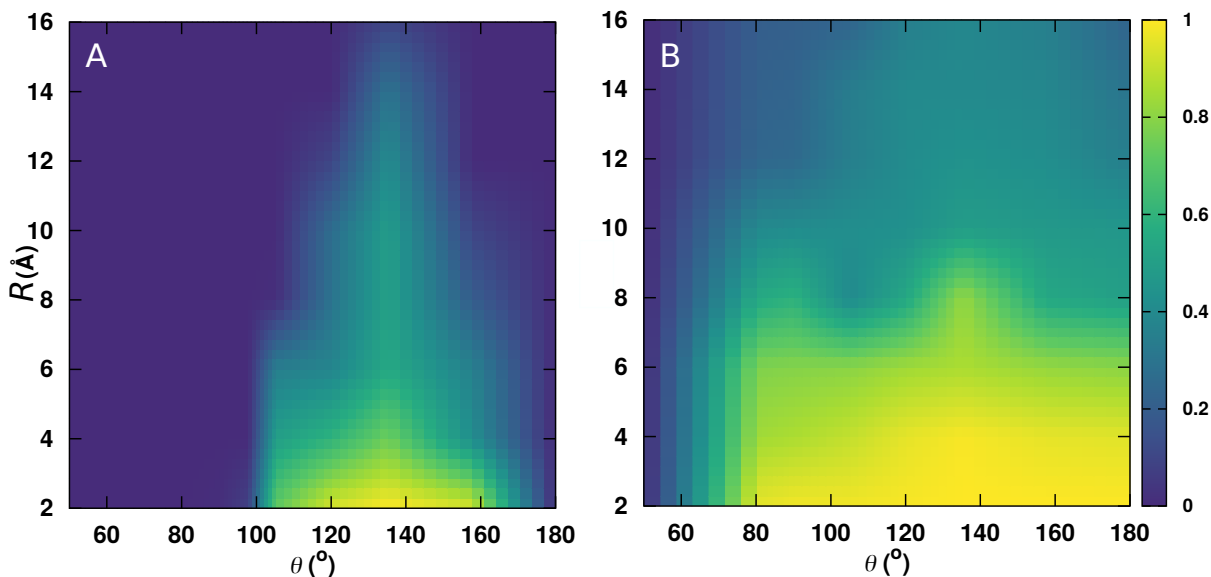


Figure 4: The NO_2 formation probability as a function of R and θ using MMH (Panel A) and RKHS (Panel B) PES. The color palette indicates the probability of the reaction, with yellow representing $P = 1$ and blue representing $P = 0$.

the 2-dimensional recombination probability using the MMH PES. For NO_2 the minima energy structure has $\theta = 134^\circ$ which leads to $P \sim 1$ for $\theta \in [125, 145]^\circ$ and $R \leq 4 \text{ \AA}$ which gradually decreases to $P \sim 0$ as R increases. Using the considerably more accurate RKHS representation the recombination probability is larger throughout, see Figure 4B. Formation probability $P \sim 1$ is found for $\theta \in [90, 180]^\circ$ and $R \leq 8 \text{ \AA}$. These differences are due to the different topographies of the two PESs. Similar to CO_2 , the recombination probability is not equal to zero at $R = 16 \text{ \AA}$ on 500 ps time scale and a plateau is observed for $R > 8 \text{ \AA}$.

Although the structures of CO_2 and NO_2 differ (linear versus bent), the shape of the underlying PES is reflected for both in geometry-dependence of the rebinding probability for shorter R . Whereas for larger distances, P is purely governed by diffusion and independent of θ .

The RKHS PES also supports the COO conformation and results in the formation and stabilization of COO. This intermediate holds significant interest as it can decay to $\text{C} + \text{O}_2$.

The probability heat map for the likelihood to form COO depending on R and θ is shown in Figure S2. Finally, the atom exchange reaction is found for 7 % of all simulation using the MMH PES for NO/CO + O. Atom exchange with RKHS is not observed for CO+O whereas 0.4 % simulations show atom exchange for NO + O collision.

3.3 Energy Dissipation upon XO₂ Relaxation

Both association reactions considered here are exothermic. Upon recombination, products are formed in a highly excited internal state (vibration and rotation) and their relaxation depends on the coupling between excited stretching/bending modes of the newly formed species and phonon and internal modes of the underlying water ice surface.⁵⁸ Ferrero et al. To allow energy transfer between the adsorbate and the internal and phonon modes of ASW, the reparametrized Burnham et al.⁶⁰, Plattner and Meuwly⁶¹ flexible Kumagai, Kawamura, and Yokokawa (KKY) water model Kumagai et al.⁶² was used in these simulations. This model had been successfully used to study vibrational relaxation of solvated cyanide Lee and Meuwly⁶³ and the relaxation of O₂ formed on ASW. Pezzella and Meuwly²¹

To study energy dissipation following recombination several hundred O+XO→XO₂ trajectories were run for 500 ps. Subsequently, 280 recombination trajectories were analyzed for CO₂ and NO₂, respectively. First, the normalized final kinetic energy distribution $P(E_{\text{kin}}^{\text{fin}})$ at 450 ps after recombination was determined for the products, see Figure S3. The $P(E_{\text{kin}}^{\text{fin}})$ for CO₂ and NO₂ extend from low- $E_{\text{kin}}^{\text{fin}}$ (~ 1 kcal/mol) to 60 kcal/mol. For NO₂ more than 80 % of the products contain $E_{\text{kin}}^{\text{fin}} < 5$ kcal/mol after 450 ps whereas for CO₂ this fraction is considerably smaller. In other words, relaxation of the highly excited internal modes is more effective for NO₂ compared with CO₂. Possible reasons for such rapid relaxation are the shallow minimum for NO₂ compared to CO₂ and/or more efficient coupling of the vibrational modes of NO₂ to the surrounding water molecules.

Next, for one CO₂-forming trajectory the kinetic energy distribution and vDOS of two water molecules W_A and W_B and the CO₂ molecule were determined for windows 1 ps in length. The time of recombination was set to zero. Water molecules W_A and W_B were chosen according to the following criterion: for the first 9 ps, W_A is the water molecule nearest to the newly formed CO₂. At 9.1 ps, the CO₂ molecule diffuses from one adsorption site on the ASW to a neighboring site which results in W_B becoming the closest water molecule. As a reference point for the analysis, the averaged E_{kin} and vDOS for 10 water molecules located away from the recombination site was determined for the 0.5 ps prior to CO₂-formation, see top row in Figure 5.

For water molecule W_A , the maximum of $P(E_{\text{kin}})$ (red shaded area) shifts to higher E_{kin} and its width increases considerably for the first 9 ps, after which relaxation to the thermal average is observed until 60 ps, see Figure 5A. In contrast, $P(E_{\text{kin}})$ for W_B (Figure 5B) remains comparable to the thermal distribution for the first 8 ps after which the position of the maximum and the width increase. This is due to energy transfer between the partially relaxed CO₂ molecule and W_B after diffusion of the CO₂. After 13 ps and until 60 ps the position of the maximum remains unchanged and the width of $P(E_{\text{kin}})$ decreases such that it reaches equilibrium again. As judged from the vDOS, the water stretch, bend and libration modes for W_A and W_B are populated for all time intervals. The two internal modes do not shift in frequency relative to the thermal equilibrium and their frequency is covered by the experimentally determined frequency range. Hagen et al.³, Yu et al.⁶⁴, Devlin⁶⁵

The CO₂ molecule formed is initially highly excited which leads to a broad, unstructured $P(E_{\text{kin}})$, top panel in Figure 5C. Over the next 9 ps the width of $P(E_{\text{kin}})$ rapidly decreases due to energy exchange with W_A and other surrounding water molecules and the phonon modes of the ASW. Cooling of CO₂ continues after diffusion to the neighboring site and

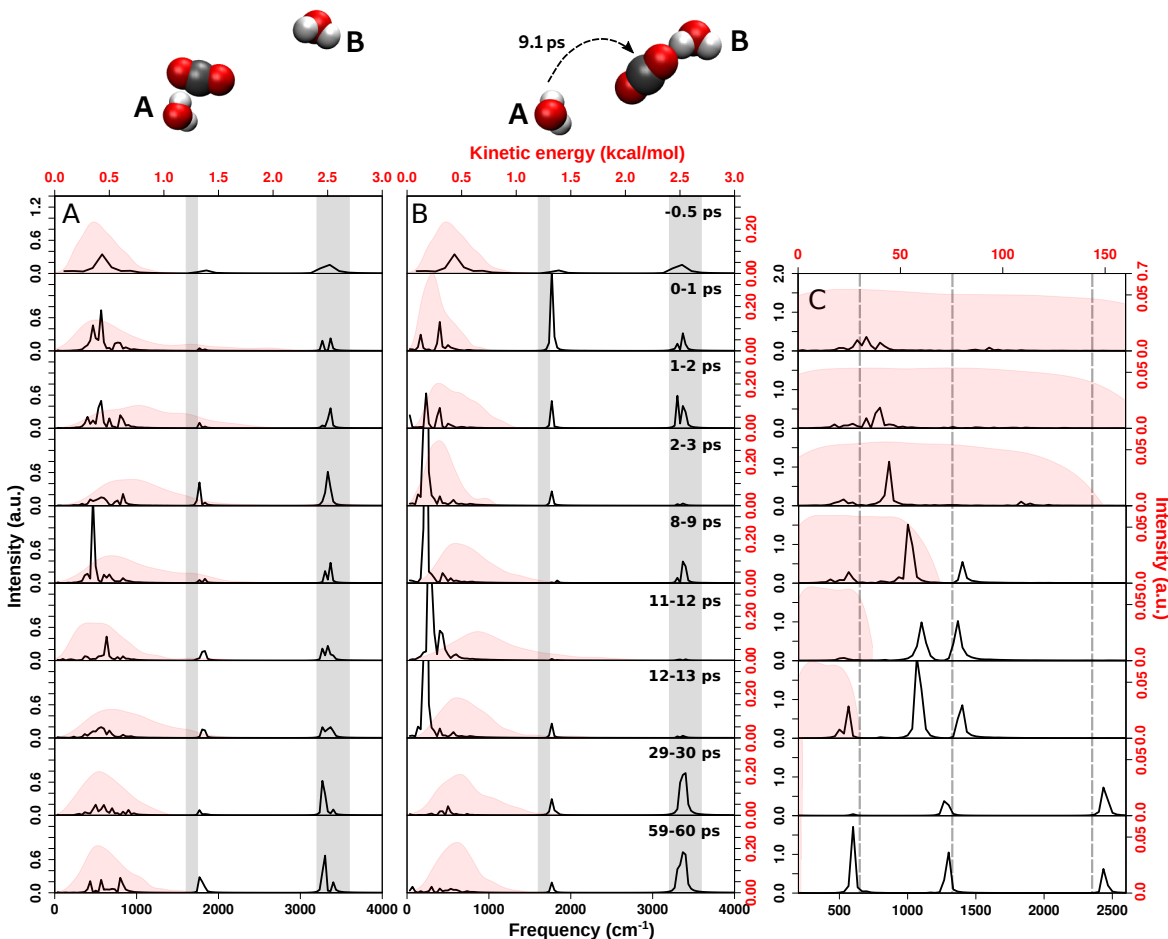


Figure 5: CO₂ recombination: The vibrational density of states power spectrum (black) and kinetic energy distribution (red) for water molecules A and B, W_A (panel A) and W_B (panel B), on the ASW surface at delay times 1, 2, 3, 9, 12, 13, 30, and 60 ps after formation of CO₂. Panel C reports the vDOS and kinetic energy distribution for CO₂. In panels A and B the shaded bands at 1600 – 1750 and 3200 – 3600 cm⁻¹ correspond to bending and OH-stretching modes. Hagen et al.³, Yu et al.⁶⁴, Devlin⁶⁵ Top panel: Averaged vDOS spectrum and kinetic energy distribution from 10 randomly chosen surface water molecules from data before recombination takes place. Subsequent panels are labeled with the time interval after CO₂ recombination.

within 60 ps after recombination the $P(E_{\text{kin}})$ for CO₂ is comparable to that of the surrounding water molecules. For the vDOS a rather different picture than for water emerges. The vibrational frequencies for CO₂ are at 667 (bend), 1333 (symmetric stretch), 2349 (antisymmetric stretch) cm⁻¹ from experiments Shimanouchi et al.⁶⁶ (see dashed vertical lines) and 647, 1374, 2353 cm⁻¹ from calculations using the reactive PES, in reasonably good agree-

ment with experiment. At the end of the observation window at 60 ps the three modes are clearly visible. However, for times shortly after recombination only frequencies below ~ 1000 cm^{-1} appear in the vDOS. Specifically, the antisymmetric stretch mode only manifests itself after 19 ps (see Figure S4 for detailed analysis) because the reactive PES for CO_2 is fully anharmonic and for the first few ps after recombination the highly excited stretching motions sample the narrowly spaced energies close to dissociation.

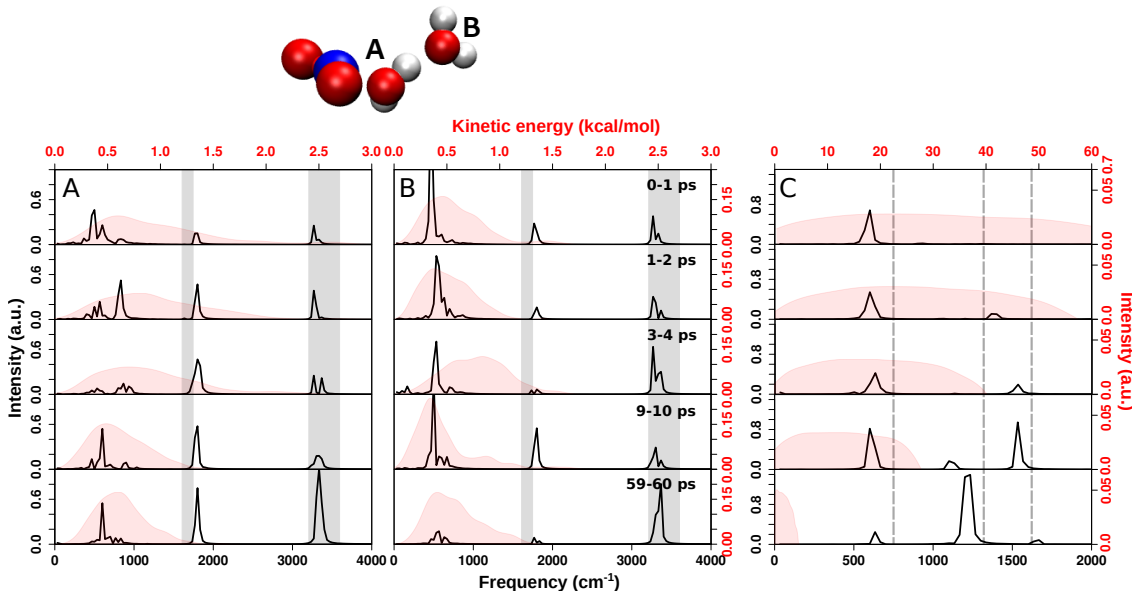


Figure 6: Vibrational density of states power spectrum (in black) and $P(E_{\text{kin}})$ (red) for water molecules A and B , W_A (panel A) and W_B (panel B), on the ASW surface at delay times 1, 2, 4, 10, and 60 ps after the formation of NO_2 . The IR bands at $1600 - 1750$ and $3200 - 3600$ cm^{-1} correspond to bending and OH-stretching modes. Hagen et al.³, Yu et al.⁶⁴, Devlin⁶⁵ Panel C reports the kinetic energy distribution (red) and the vDOS of the NO_2 molecule.

For studying energy transfer between neighboring water molecules on the ASW, a slightly different approach was used for NO_2 recombination. For one NO_2 -forming trajectory, the kinetic energy distribution and vDOS of water molecules W_A and W_B and NO_2 were determined. Here, W_A represents the water molecule closest to NO_2 , while W_B is nearest to W_A , see Figure 6. For W_A the width of $P(E_{\text{kin}})$ is considerably broader than the thermal distribution already for the first ps (0-1 ps), see top panel in Figure 6A, and narrow only at

9 ps after recombination. In contrast, $P(E_{\text{kin}})$ for W_B which is not in direct contact with the recombining NO_2 is initially comparable to thermal equilibrium but widens after 3 ps (Figure 6B). Within the next 6 ps the width decreases again and equilibrium is established within 60 ps for both water molecules. The peak maxima shift to higher E_{kin} at early times and develop towards thermal equilibrium on the 60 ps time scale. The kinetic energy distribution for NO_2 starts out broad (60 kcal/mol) and transfers more than half of this energy to the environment within 10 ps of recombination (Figure 6C). Within 60 ps $P(E_{\text{kin}})$ is close to thermal equilibrium.

The experimentally measured Arakawa and Nielsen⁶⁷ vibrational frequencies for gas phase NO_2 are at 750 (bend), 1318 (symmetric stretch), 1618 (antisymmetric stretch) cm^{-1} . A blue shift over time is observed as the NO_2 molecule loses energy. After 60 ps, it begins to probe the low-energy regions of the potential, revealing distinct peaks. For NO_2 , the final E_{kin} fluctuates around ~ 5 kcal/mol, causing the peak to shift from its equilibrium features. During the initial picoseconds, there is a notable population in the region of the water libration modes compared to bending and stretching. However beyond 60 ps, as the system approaches equilibrium, the range of the libration modes is less populated/unpopulated. In contrast, the stretching modes gain intensity.

Comparing specifically the time evolution of $P(E_{\text{kin}})$ for CO_2 and NO_2 it is observed that the two products differ in the efficiency and speed of cooling. For NO_2 the fraction of products formed with $E_{\text{kin}} \sim 5$ kcal/mol within ~ 500 ps is twice as large compared with CO_2 . This may be related to the lower energy of formation (3.24 eV vs. 7.71 eV) but also due to the overall lower vibrational energies of the fundamentals for NO_2 compared with CO_2 .

For a more mode-specific analysis of energy transfer between the formed CO_2 and the surrounding water molecules the time evolution of the integrated vDOS in three frequency

ranges was considered. These frequency ranges correspond to water libration ($0 - 1000 \text{ cm}^{-1}$), bending ($1500 - 2000 \text{ cm}^{-1}$) and stretching ($2800 - 3800 \text{ cm}^{-1}$), in Figures 5 and 6. For analysis, water molecules within 10 \AA in the x -direction and 5 \AA in the y/z -direction located around the recombination site were used, see Figure S5. Then the vibrational density of states (vDOS) was computed for each water molecule separately, and the resulting peak areas were averaged over 100 water molecules. Figure 7A reports the difference between the equilibrium averaged peak area and the area at time t after recombination. For better comparison, the difference between peak area right after excitation and the area at time t is shown in Panel B. The integrated intensity of the low-frequency libration mode (black line) initially increases, followed by a decrease after 12 ps, and eventually reaching a plateau. Meanwhile, the intensity of the stretching modes (green) displays a progressive rise over the first 50 ps, followed by fluctuations around a specific value. In comparison, the intensity of bending modes remains comparable throughout the observed time frame (similar observation in Figure S6). The time series show that the libration mode first acquires and stores energy and subsequently releases it, whereas the stretching modes pick up energy on the 100 ps time scale and retain it beyond that. This was also observed for NH_3 formation on water ice. Ferrero et al.⁵⁸

3.4 Species Desorption on ASW

To explicitly probe desorption, velocities for the adsorbants (CO , NO , CO_2 , and NO_2) were drawn from a Maxwell-Boltzmann distribution and scaled along the x -direction, perpendicular to the water surface. Pezzella et al.⁵² For the water molecules the velocities were those from an equilibrium simulation at 50 K and the dynamics of the system was followed for 100 ps. If within this time scale the adsorbant remained on the ASW, it was considered physisorbed. However, for sufficiently large scaling of the velocity vector the adsorbant leaves the ASW from which the desorption energy can be estimated. Pezzella et al.⁵² Average des-

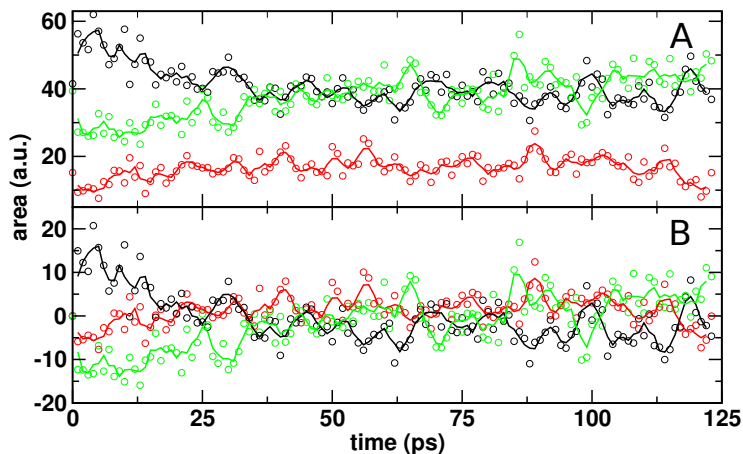


Figure 7: Time evolution of the integrated change of vDOS curves averaged over 100 water molecules for libration (black), bending (red), and stretching modes (green) of water. In Panel A, the equilibrium, thermally averaged area before recombination is the reference for calculating the difference at time t whereas for Panel B the peak area right after excitation ($t = 1$ ps) is the reference. Here, solid lines represent the 4-point moving average.

orption energies were determined from initiating the dynamics for different initial positions of the adsorbant on the ASW.

Computed desorption energies (E_{des}) for CO and NO from the ASW surface were 3.5 ± 0.7 kcal/mol (1812 K or 156 meV) and 3.1 ± 0.5 kcal/mol (1534 K or 132 meV), respectively. Earlier MD simulations reported⁵³ CO-desorption energies between 3.1 and 4.0 kcal/mol (1560 K to 2012 K or 130 meV to 170 meV), compared with 120 meV (2.8 kcal/mol or 1392 K) from experiments. Karssemeijer et al.⁶⁸ It was also found that the desorption energy of CO from ASW depends on CO coverage with ranges from $E_{\text{des}} = 1700$ K for low to $E_{\text{des}} = 1000$ K for high coverage, respectively, He et al.⁷ which supports the simulation results.⁵³ On non-porous and crystalline water surfaces submonolayer desorption energies for CO are 1307 K and 1330 K (~ 115 meV), respectively. Noble et al.⁶⁹ For NO, experiments found a desorption energy of 1300 K (2.6 kcal/mol or 112 meV) using temperature programmed desorption measurements Minissale et al.⁷⁰ after exposure of NO/H₂O ice to atomic oxygen. Thus, for both diatomics the present findings are consistent with experiments and earlier simulations.

For the triatomics, average desorption energies for CO₂ and NO₂ from ASW were 9.0 ± 1.9 kcal/mol (4529 K or 390 meV) and 13.1 ± 3.4 kcal/mol (6592 K and 568 meV). For CO₂ one experiment reported $E_{\text{des}} = 2490 \pm 240$ K Galvez et al.⁷¹ (4.9 ± 0.47 kcal/mol or 214 ± 20 meV) and a compilation of literature data reports values between 4.5 and 6.0 kcal/mol. Wakelam et al.⁷² On the other hand, for NO₂ no experimentally measured data is available; Wakelam et al.⁷² however, the desorption temperatures of NO₂ and H₂O from the same ice surface were found to be comparable which indicates that NO₂ interacts strongly with the surface. Ioppolo et al.⁷³ Overall, for all four species relevant to the present work the computed E_{des} compare reasonably (CO₂) to favourably (CO, NO) with reference values from experiments and previous calculations, particularly in light of the fact that appreciable variations in experimentally reported values exist. Wakelam et al.⁷²

3.5 Species Diffusion on ASW

To determine typical diffusion barrier heights, a 30 ns long simulation of molecules (CO, NO, CO₂, and NO₂) on water surface was run with velocities from a Maxwell-Boltzmann distribution at 50 K. For each frame, their interaction energy with the ASW surface was determined and mapped onto the ASW surface to give a 2-dimensional map, see Figures 8 and S7. Figure 8A shows the 2D projection of CO interaction energy with ASW from a 30 ns long simulation. The black solid line traces the path followed by the CO molecule on top of the ASW surface. The total path length with several minima enumerated and the interaction energy between CO and the ASW is reported in Figure 8B. The diffusion barrier heights vary between minima and are a consequence of ASW surface roughness. Pezzella et al.²⁰ On average, the activation barrier for diffusion between neighboring minima is 1.15 kcal/mol. Experimentally, a range of diffusion barriers was found to extend from $E_b \sim 120 \pm 180$ K to 490 ± 12 K. Kouchi et al.⁸, Acharyya⁷⁴ Another study reported E_b separately for weakly and strongly bound sites to be ~ 350 K and ~ 930 K, respectively. Karssemeijer and Cuppen⁷⁵

Hence, experimentally the diffusion barriers range from 0.25 kcal/mol to 1.85 kcal/mol. The present simulations support a distribution of barriers and are consistent with the experimentally reported values.

The calculated average activation barrier for diffusion of NO (Figure S7A) between neighboring minima is 0.91 kcal/mol. From equilibrium trajectories at 50 K no diffusion for CO₂ and NO₂ on the 75 ns time scale is observed. For CO₂ one experiment reported an average diffusion barrier of 2150 K (4.3 kcal/mol).⁷⁶ He et al. As a comparison, for CO the average diffusion barrier height is ~ 1 kcal/mol which leads to a transition time between neighboring minima of ~ 1 ns. Within an Arrhenius picture for surface diffusion - which may not be entirely appropriate at sufficiently low temperatures²⁰ - a barrier of ~ 4 kcal/mol corresponds to a diffusion time scale on the order of several hundred ns. This is consistent with the present findings that on the sub-100 ns time scale CO₂ does not diffuse on ASW. For comparison, the diffusion of CO₂ and NO₂ on the water surface after recombination is shown in Figure S8.

Earlier work already demonstrated that oxygen diffusion coefficients are consistent with the experiment. Atomic oxygen²⁰ on ASW experiences diffusional barriers between $E_{\text{dif}} = 0.2$ kcal/mol and 2 kcal/mol (100 K to 1000 K) compared with an averaged value of $E_{\text{dif}} = 990_{-360}^{+530}$ K determined from experiments.³⁰ Minissale et al.

4 Discussion and Conclusion

The present work underlines that larger molecules can form and stabilize from atomic and molecular constituents on ASW. The rate-limiting step for CO₂- and NO₂-generation is the diffusion of the reactant species. After recombination, both products efficiently cool on

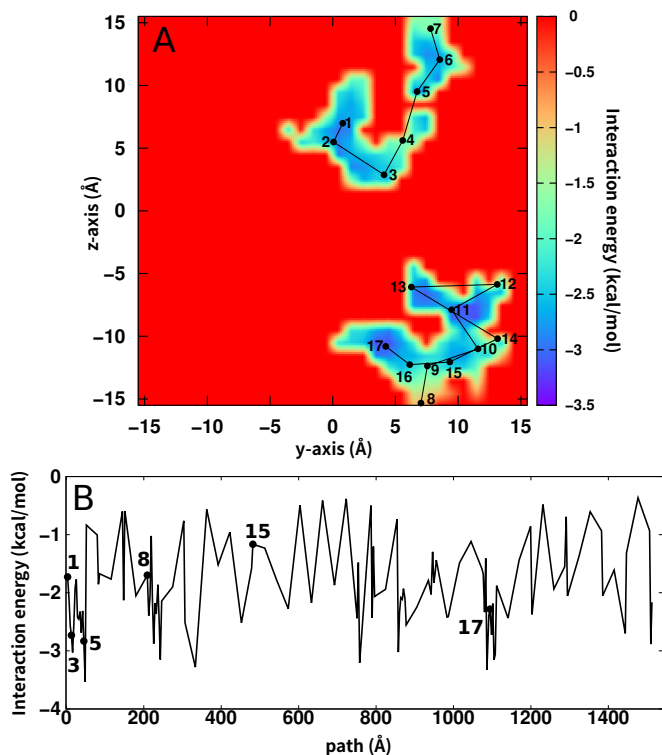


Figure 8: Diffusion of CO on ASW. Panel A: 2D projection of CO interaction energy and diffusion path onto the ASW $y - z$ plane from a 30 ns long simulation at 50 K. Panel B: 1D projection of the path followed with some of the minima visited in panel A labeled with corresponding numbers. Between minima 15 and 17 the adsorbant repeatedly visits minima 8 to 17. The average diffusion barrier height is 1.15 kcal/mol compared with a range from 0.25 kcal/mol to 1.85 kcal/mol from experiments. Acharyya⁷⁴, Karssemeijer and Cuppen⁷⁵

the 10 picosecond time scale although a smaller fraction still remains in an internally hot state. Use of a fluctuating charge model clarifies that on the nanosecond time scale recombination can occur from atom-molecule separations up to $\sim 20 \text{ \AA}$. Given the much longer time scales available in interstellar chemistry the areas covered by the reactants will increase in proportion. The energy liberated upon recombination is efficiently transferred into water-internal modes and lattice vibrations (phonons) on the picosecond time scale. Of particular note is the vanishingly small equilibrium diffusivity of CO_2 and NO_2 at low temperatures (here 50 K) which is consistent with experiment, whereas immediately after recombination the triatomics diffuse and roam wider parts of the ASW.

Astrophysical implications of the present work include physical and chemical aspects alike.

Recombination reactions liberate energy to drive restructuring of the underlying surface. As a consequence of recombination local heating of the ASW can take place which also potentially increases the local diffusivity and leads to desorption of reactive species such as H or OH. This is particularly relevant as the cold average temperatures of ~ 10 K restrict motion to the lightest particles or driven by tunneling only.⁷⁷ Because the surface morphology in part determines its chemical activity, reconfiguration of the solid support is an important determinant for downstream reactivity. The simulations also show that following recombination, products undergo nonthermal surface diffusion (see Figure S8) which leads to mass transport across the surface to initiate chemistry at other locations. This is particularly relevant because products can remain in an internally excited state that can lead to breakup and radical formation.

In summary, the present work establishes that triatomics can be formed and stabilized following atom+diatom recombination reactions. The kernel-based potential energy surfaces combined with physically meaningful electrostatic models allow to run statistically significant numbers of trajectories and provide molecular-level insight into energy relaxation and redistribution. This work provides a basis for broader reaction exploration on ASW, in particular in light of recent progress to represent high-dimensional, reactive PESs based on neural networks.⁷⁸

Acknowledgments

The authors gratefully acknowledge financial support from the Swiss National Science Foundation through grant 200020_188724 and to the NCCR-MUST.

References

- (1) Herbst, E. The chemistry of interstellar space. *Chem. Soc. Rev.* **2001**, *30*, 168–176.
- (2) Wakelam, V.; Bron, E.; Cazaux, S.; Dulieu, F.; Gry, C.; Guillard, P.; Habart, E.; Hornekær, L.; Morisset, S.; Nyman, G., et al. H₂ formation on interstellar dust grains: The viewpoints of theory, experiments, models and observations. *Mol. Astrophys.* **2017**, *9*, 1–36.
- (3) Hagen, W.; Tielens, A.; Greenberg, J. The infrared spectra of amorphous solid water and ice Ic between 10 and 140 K. *Chem. Phys.* **1981**, *56*, 367–379.
- (4) Jenniskens, P.; Blake, D. Structural transitions in amorphous water ice and astrophysical implications. *Science* **1994**, *265*, 753–756.
- (5) Bossa, J. B.; Isokoski, K.; de Valois, M. S.; Linnartz, H. Thermal collapse of porous interstellar ice. *Astron. Astrophys.* **2012**, *545*, A82.
- (6) Bar-Nun, A.; Dror, J.; Kochavi, E.; Laufer, D. Amorphous water ice and its ability to trap gases. *Phys. Rev. B* **1987**, *35*, 2427–2435.
- (7) He, J.; Acharyya, K.; Vidali, G. Binding Energy of Molecules on Water Ice: Laboratory Measurements and Modeling. *Astrophys. J.* **2016**, *825*, 89.
- (8) Kouchi, A.; Furuya, K.; Hama, T.; Chigai, T.; Kozasa, T.; Watanabe, N. Direct Measurements of Activation Energies for Surface Diffusion of CO and CO₂ on Amorphous Solid Water Using In Situ Transmission Electron Microscopy. *Astrophys. J. Lett.* **2020**, *891*, L22.
- (9) Oba, Y.; Miyauchi, N.; Hidaka, H.; Chigai, T.; Watanabe, N.; Kouchi, A. Formation of Compact Amorphous H₂O Ice by Codeposition of Hydrogen Atoms with Oxygen Molecules on Grain Surfaces. *Astrophys. J.* **2009**, *701*, 464–470.

- (10) Keane, J.; Tielens, A.; Boogert, A.; Schutte, W.; Whittet, D. Ice absorption features in the 5-8 μm region toward embedded protostars. *Astron. Astrophys.* **2001**, *376*, 254–270.
- (11) Kouchi, A.; Tsuge, M.; Hama, T.; Oba, Y.; Okuzumi, S.; Sirono, S.-i.; Momose, M.; Nakatani, N.; Furuya, K.; Shimonishi, T., et al. Transmission Electron Microscopy Study of the Morphology of Ices Composed of H_2O , CO_2 , and CO on Refractory Grains. *Astrophys. J.* **2021**, *918*, 45.
- (12) Bossa, J.-B.; Isokoski, K.; Paardekooper, D. M.; Bonnin, M.; van der Linden, E. P.; Triemstra, T.; Cazaux, S.; Tielens, A. G. G. M.; Linnartz, H., Porosity measurements of interstellar ice mixtures using optical laser interference and extended effective medium approximations. *Astron. Astrophys.* **2014**, *561*, A136.
- (13) Bossa, J.-B.; Maté, B.; Fransen, C.; Cazaux, S.; Pilling, S.; Rocha, W. R. M.; Ortigoso, J.; Linnartz, H. Porosity and band-strength measurements of multi-phase composite ices. *Astrophys. J.* **2015**, *814*, 47.
- (14) Cazaux, S.; Bossa, J.-B.; Linnartz, H.; Tielens, A. G. G. M., Pore evolution in interstellar ice analogues - Simulating the effects of temperature increase. *Astron. Astrophys.* **2015**, *573*, A16.
- (15) Ioppolo, S.; Cuppen, H. M.; Linnartz, H. Surface formation routes of interstellar molecules: hydrogenation reactions in simple ices. *Rend. Lincei.* **2011**, *22*, 211–224.
- (16) Romanzin, C.; Ioppolo, S.; Cuppen, H. M.; van Dishoeck, E. F.; Linnartz, H. Water formation by surface O_3 hydrogenation. *J. Chem. Phys.* **2011**, *134*, 084504.
- (17) Chaabouni, H.; Minissale, M.; Manicò, G.; Congiu, E.; Noble, J. A.; Baouche, S.; Accolla, M.; Lemaire, J. L.; Pirronello, V.; Dulieu, F. Water formation through $\text{O}_2 + \text{D}$ pathway on cold silicate and amorphous water ice surfaces of interstellar interest. *J. Chem. Phys.* **2012**, *137*, 234706.

- (18) Minissale, M.; Congiu, E.; Baouche, S.; Chaabouni, H.; Moudens, A.; Dulieu, F.; Accolla, M.; Cazaux, S.; Manico, G.; Pirronello, V. Quantum Tunneling of Oxygen Atoms on Very Cold Surfaces. *Phys. Rev. Lett.* **2013**, *111*, 053201.
- (19) Dulieu, F.; Minissale, M.; Bockelée-Morvan, D., Production of O₂ through dismutation of H₂O₂ during water ice desorption: a key to understanding comet O₂ abundances. *Astron. Astrophys.* **2017**, *597*, A56.
- (20) Pezzella, M.; Unke, O. T.; Meuwly, M. Molecular Oxygen Formation in Interstellar Ices Does Not Require Tunneling. *J. Phys. Chem. Lett.* **2018**, *9*, 1822–1826.
- (21) Pezzella, M.; Meuwly, M. O₂ formation in cold environments. *Phys. Chem. Chem. Phys.* **2019**, *21*, 6247–6255.
- (22) Christianson, D. A.; Garrod, R. T. Chemical Kinetics Simulations of Ice Chemistry on Porous Versus Non-Porous Dust Grains. *Front. astron. space sci.* **2021**, *8*, 643297.
- (23) Hama, T.; Watanabe, N. Surface Processes on Interstellar Amorphous Solid Water: Adsorption, Diffusion, Tunneling Reactions, and Nuclear-Spin Conversion. *Chem. Rev.* **2013**, *113*, 8783–8839.
- (24) Minissale, M.; Congiu, E.; Manicò, G.; Pirronello, V.; Dulieu, F. CO₂ formation on interstellar dust grains: a detailed study of the barrier of the CO channel. *Astron. Astrophys.* **2013**, *559*, A49.
- (25) Minissale, M.; Moudens, A.; Baouche, S.; Chaabouni, H.; Dulieu, F. Hydrogenation of CO-bearing species on grains: unexpected chemical desorption of CO. *Mon. Not. Roy. Astron. Soc.* **2016**, *458*, 2953–2961.
- (26) Qasim, D.; Fedoseev, G.; Chuang, K.-J.; He, J.; Ioppolo, S.; van Dishoeck, E.; Linartz, H. An experimental study of the surface formation of methane in interstellar molecular clouds. *Nat. Astron.* **2020**, *4*, 781–785.

- (27) Molpeceres, G.; Kästner, J.; Fedoseev, G.; Qasim, D.; Schömig, R.; Linnartz, H.; Lamberts, T. Carbon Atom Reactivity with Amorphous Solid Water: H₂O-Catalyzed Formation of H₂CO. *J. Phys. Chem. Lett.* **2021**, *12*, 10854–10860.
- (28) Minissale, M.; Fedoseev, G.; Congiu, E.; Ioppolo, S.; Dulieu, F.; Linnartz, H. Solid state chemistry of nitrogen oxides – Part I: surface consumption of NO. *Phys. Chem. Chem. Phys.* **2014**, *16*, 8257–8269.
- (29) Minissale, M.; Nguyen, T.; Dulieu, F., Experimental study of the penetration of oxygen and deuterium atoms into porous water ice. *Astron. Astrophys.* **2019**, *622*, A148.
- (30) Minissale, M.; Congiu, E.; Dulieu, F. Direct measurement of desorption and diffusion energies of O and N atoms physisorbed on amorphous surfaces. *Astron. Astrophys.* **2016**, *585*, A146.
- (31) Tsuge, M.; Hidaka, H.; Kouchi, A.; Watanabe, N. Diffusive Hydrogenation Reactions of CO Embedded in Amorphous Solid Water at Elevated Temperatures 70 K. *Astrophys. J.* **2020**, *900*, 187.
- (32) Lee, M. W.; Meuwly, M. Diffusion of atomic oxygen relevant to water formation in amorphous interstellar ices. *Faraday Discuss.* **2014**, *168*, 205–222.
- (33) Roser, J. E.; Vidali, G.; Manicò, G.; Pirronello, V. Formation of carbon dioxide by surface reactions on ices in the interstellar medium. *Astrophys. J. Lett.* **2001**, *555*, L61.
- (34) Liszt, H.; Turner, B. Microwave detection of interstellar NO. *Astrophys. J.* **1978**, *224*, L73–L76.
- (35) Ligterink, N. F. W.; Calcutt, H.; Coutens, A.; Kristensen, L.; Bourke, T.; Drozdovskaya, M. N.; Müller, H.; Wampfler, S.; van Der Wiel, M.; Van Dishoeck, E., et al.

- The ALMA-PILS survey: Stringent limits on small amines and nitrogen-oxides towards IRAS 16293–2422B. *Astron. Astrophys.* **2018**, *619*, A28.
- (36) Codella, C.; Viti, S.; Lefloch, B.; Holdship, J.; Bachiller, R.; Bianchi, E.; Ceccarelli, C.; Favre, C.; Jiménez-Serra, I.; Podio, L., et al. Nitrogen oxide in protostellar envelopes and shocks: the ASAI survey. *Mon. Notices Royal Astron. Soc.* **2018**, *474*, 5694–5703.
- (37) Ziurys, L.; McGonagle, D.; Minh, Y.; Irvine, W. Nitric oxide in star-forming regions—Further evidence for interstellar NO bonds. *Astrophys. J.* **1991**, *373*, 535–542.
- (38) McGonagle, D.; Ziurys, L.; Irvine, W. M.; Minh, Y. Detection of nitric oxide in the dark cloud L134N. *Astrophys. J.* **1990**, *359*, 121–124.
- (39) Ziurys, L.; Apponi, A.; Hollis, J.; Snyder, L. Detection of interstellar N₂O: A new molecule containing an NO bond. *Astrophys. J.* **1994**, *436*, L181–L184.
- (40) Snyder, L. E.; Kuan, Y.-J.; Ziurys, L.; Hollis, J. New 3 millimeter observations of interstellar HNO—Reinstating a discredited identification. *Astrophys. J.* **1993**, *403*, L17–L20.
- (41) de Barros, A.; Da Silveira, E.; Fulvio, D.; Boduch, P.; Rothard, H. Formation of nitrogen-and oxygen-bearing molecules from radiolysis of nitrous oxide ices—implications for Solar system and interstellar ices. *Mon. Notices Royal Astron. Soc.* **2016**, *465*, 3281–3290.
- (42) Congiu, E.; Fedoseev, G.; Ioppolo, S.; Dulieu, F.; Chaabouni, H.; Baouche, S.; Lemaire, J. L.; Laffon, C.; Parent, P.; Lamberts, T., et al. No ice hydrogenation: a solid pathway to NH₂OH formation in space. *Astrophys. J. Lett.* **2012**, *750*, L12.
- (43) Stief, L. J.; Payne, W. A.; Klemm, R. B. A flash photolysis–resonance fluorescence study of the formation of O(¹D) in the photolysis of water and the reaction of O(¹D) with H₂, Ar, and He-. *J. Chem. Phys.* **1975**, *62*, 4000–4008.

- (44) Garstang, R. Energy levels and transition probabilities in p^2 and p^4 configurations. *Mon. Not. R. Astron. Soc.* **1951**, *111*, 115–124.
- (45) Schmidt, F.; Swiderek, P.; Bredehoöft, J. H. Formation of Formic Acid, Formaldehyde, and Carbon Dioxide by Electron-Induced Chemistry in Ices of Water and Carbon Monoxide. *ACS Earth Space Chem.* **2019**, *3*, 1974–1986.
- (46) Chou, S.-L.; Lo, J.-I.; Peng, Y.-C.; Lu, H.-C.; Cheng, B.-M.; Ogilvie, J. F. Photolysis of O_2 dispersed in solid neon with far-ultraviolet radiation. *Phys. Chem. Chem. Phys.* **2018**, *20*, 7730–7738.
- (47) T. Nagy, J. Y. R.; Meuwly, M. Multi-Surface Adiabatic Reactive Molecular Dynamics. *J. Chem. Theo. Comp.* **2014**, *10*, 1366–1375.
- (48) Werner, H.-J. et al. The Molpro quantum chemistry package. *J. Chem. Phys.* **2020**, *152*, 144107.
- (49) Werner, H.-J.; Knowles, P. J. An efficient internally contracted multiconfiguration–reference configuration interaction method. *J. Chem. Phys.* **1988**, *89*, 5803–5814.
- (50) Dunning Jr, T. H. Gaussian basis sets for use in correlated molecular calculations. I. The atoms boron through neon and hydrogen. *J. Chem. Phys.* **1989**, *90*, 1007–1023.
- (51) Best, R. B.; Zhu, X.; Shim, J.; Lopes, P. E.; Mittal, J.; Feig, M.; MacKerell Jr, A. D. Optimization of the additive CHARMM all-atom protein force field targeting improved sampling of the backbone ϕ , ψ and side-chain χ_1 and χ_2 dihedral angles. *J. Chem. Theo. Comp.* **2012**, *8*, 3257–3273.
- (52) Pezzella, M.; Koner, D.; Meuwly, M. Formation and Stabilization of Ground and Excited-State Singlet O_2 upon Recombination of 3P Oxygen on Amorphous Solid Water. *J. Phys. Chem. Lett.* **2020**, *11*, 2171–2176.

- (53) Upadhyay, M.; Pezzella, M.; Meuwly, M. Genesis of Polyatomic Molecules in Dark Clouds: CO₂ Formation on Cold Amorphous Solid Water. *J. Phys. Chem. Lett.* **2021**, *12*, 6781–6787.
- (54) San Vicente Veliz, J. C.; Koner, D.; Schwilk, M.; Bemish, R. J.; Meuwly, M. The N(⁴S) + O₂(X³Σ) \longleftrightarrow O(³P) + NO(X²Π) Reaction: Thermal and Vibrational Relaxation Rates for the ²A', ⁴A' and ²A" States. *Phys. Chem. Chem. Phys.* **2020**, *22*, 3927–3939.
- (55) Brooks, B. et al. CHARMM: the biomolecular simulation program. *J. Comp. Chem.* **2009**, *30*, 1545–614.
- (56) Unke, O. T.; Meuwly, M. Toolkit for the Construction of Reproducing Kernel-Based Representations of Data: Application to Multidimensional Potential Energy Surfaces. *J. Chem. Inf. Model.* **2017**, *57*, 1923–1931.
- (57) Gageot, M.-P.; Martinez, M.; Vuilleumier, R. Infrared spectroscopy in the gas and liquid phase from first principle molecular dynamics simulations: application to small peptides. *Mol. Phys.* **2007**, *105*, 2857–2878.
- (58) Ferrero, S.; Pantaleone, S.; Ceccarelli, C.; Ugliengo, P.; Sodupe, M.; Rimola, A. Where does the energy go during the interstellar NH₃ formation on water ice? A computational study. *Astrophys. J.* **2023**, *944*, 142.
- (59) Futrelle, R.; McGinty, D. Calculation of spectra and correlation functions from molecular dynamics data using the fast Fourier transform. *Chemical Physics Letters* **1971**, *12*, 285–287.
- (60) Burnham, C. J.; Li, J. C.; Leslie, M. Molecular Dynamics Calculations for Ice Ih. *J. Phys. Chem. B* **1997**, *101*, 6192–6195.
- (61) Plattner, N.; Meuwly, M. Atomistic Simulations of CO Vibrations in Ices Relevant to Astrochemistry. *ChemPhysChem* **2008**, *9*, 1271–1277.

- (62) Kumagai, N.; Kawamura, K.; Yokokawa, T. An Interatomic Potential Model for H₂O: Applications to Water and Ice Polymorphs. *Mol. Sim.* **1994**, *12*, 177–186.
- (63) Lee, M. W.; Meuwly, M. On the role of nonbonded interactions in vibrational energy relaxation of cyanide in water. *J. Phys. Chem. A* **2011**, *115*, 5053–5061.
- (64) Yu, C.-C.; Chiang, K.-Y.; Okuno, M.; Seki, T.; Ohto, T.; Yu, X.; Korepanov, V.; Hamaguchi, H.-o.; Bonn, M.; Hunger, J., et al. Vibrational couplings and energy transfer pathways of water’s bending mode. *Nat. Commun.* **2020**, *11*, 5977.
- (65) Devlin, J. P. Vibrational modes of amorphous ice: bending mode frequencies for isotopically decoupled H₂O and HOD at 90 K. *J. Mol. Struct.* **1990**, *224*, 33–43.
- (66) Shimanouchi, T.; Matsuura, H.; Ogawa, Y.; Harada, I. Tables of molecular vibrational frequencies. *J. Phys. Chem. Ref. Data* **1978**, *7*, 1323–1444.
- (67) Arakawa, E. T.; Nielsen, A. H. Infrared spectra and molecular constants of N¹⁴O₂ and N¹⁵O₂. *J. Mol. Spectrosc.* **1958**, *2*, 413–427.
- (68) Karssemeijer, L.; Ioppolo, S.; van Hemert, M.; van der Avoird, A.; Allodi, M.; Blake, G.; Cuppen, H. Dynamics of CO in amorphous water-ice environments. *Astrophys. J.* **2013**, *781*, 1–15.
- (69) Noble, J.; Congiu, E.; Dulieu, F.; Fraser, H. Thermal desorption characteristics of CO, O₂ and CO₂ on non-porous water, crystalline water and silicate surfaces at submonolayer and multilayer coverages. *Mon. Not. R. Astron. Soc.* **2012**, *421*, 768–779.
- (70) Minissale, M.; Nguyen, T.; Dulieu, F. Experimental study of the penetration of oxygen and deuterium atoms into porous water ice. *Astron. Astrophys.* **2019**, *622*, A148.
- (71) Galvez, O.; Ortega, I. K.; Maté, B.; Moreno, M. A.; Martín-Llorente, B.; Herrero, V. J.; Escribano, R.; Gutiérrez, P. J. A study of the interaction of CO₂ with water ice. *Astron. Astrophys.* **2007**, *472*, 691–698.

- (72) Wakelam, V.; Loison, J.-C.; Mereau, R.; Ruaud, M. Binding energies: New values and impact on the efficiency of chemical desorption. *Mol. Astrophys.* **2017**, *6*, 22–35.
- (73) Ioppolo, S.; Fedoseev, G.; Minissale, M.; Congiu, E.; Dulieu, F.; Linnartz, H. Solid state chemistry of nitrogen oxides–Part II: surface consumption of NO₂. *Phys. Chem. Chem. Phys.* **2014**, *16*, 8270–8282.
- (74) Acharyya, K. Understanding the impact of diffusion of CO in the astrochemical models. *Pub. Astron. Soc. Austr.* **2022**, *39*, e009.
- (75) Karssemeijer, L.; Cuppen, H. Diffusion-desorption ratio of adsorbed CO and CO₂ on water ice. *Astron. Astrophys.* **2014**, *569*, A107.
- (76) He, J.; Emtiaz, S.; Vidali, G. Measurements of Diffusion of Volatiles in Amorphous Solid Water: Application to Interstellar Medium Environments. *Astrophys. J.* **2018**, *863*, 156.
- (77) Fredon, A.; Lamberts, T.; Cuppen, H. Energy dissipation and nonthermal diffusion on interstellar ice grains. *Astrophys. J.* **2017**, *849*, 125.
- (78) Upadhyay, M.; Topfer, K.; Meuwly, M. Molecular Simulation for Atmospheric Reactions: Non-Equilibrium Dynamics, Roaming, and Glycolaldehyde Formation following Photoinduced Decomposition of syn-Acetaldehyde Oxide. *J. Phys. Chem. Lett.* **2023**, *15*, 90–96.

Supporting Information: Oxygenation of CO and NO on Amorphous Solid Water

Meenu Upadhyay[†] and Markus Meuwly^{*,‡}

[†]*Department of Chemistry, University of Basel, Klingelbergstrasse 80, CH-4056 Basel, Switzerland.*

[‡]*Department of Chemistry, University of Basel, Klingelbergstrasse 80, CH-4056 Basel, Switzerland.*

E-mail: m.meuwly@unibas.ch

March 25, 2024

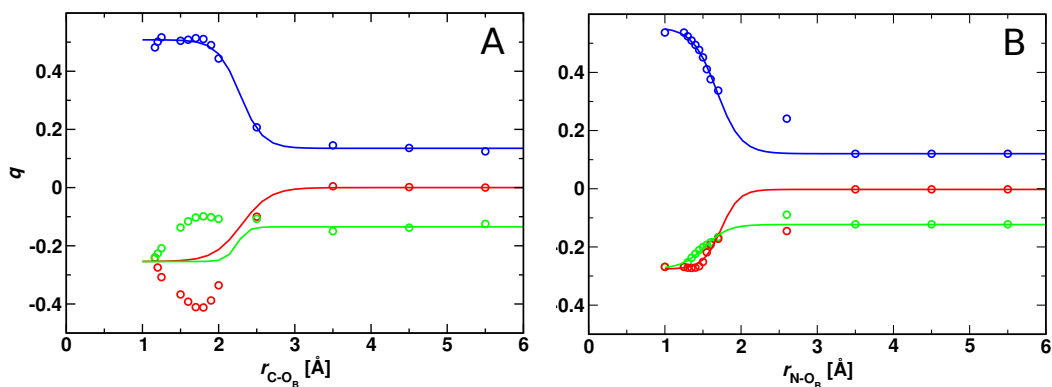


Figure S1: Change in charges of the atoms adsorbed to the 10 nearest H₂O molecules during CO₂/NO₂ formation as a function of $r(\text{C/N-O}_B)$ Å distance. Panels A and B correspond to CO₂ and NO₂, respectively. At low temperatures, the reaction probability completely depends on the diffusion of species for which charges fit well at asymptotic. At close range ($r \sim 2$ Å and shorter) bonded interactions dominate. Finally, at equilibrium, correct charges are achieved by the fitted function. Filled circles and solid line refers to *ab initio* determined and fitted charges, respectively. Color code: C/N atoms (blue) and atomic oxygen O_B (red).

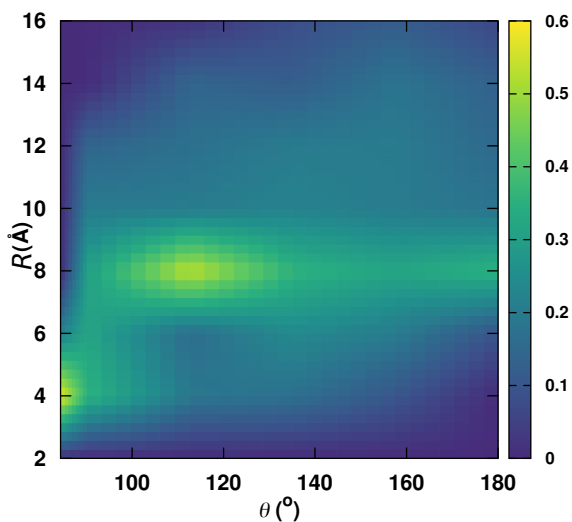


Figure S2: KDE density map for the average COO formation probability depending on initial (R, θ) using RKHS PES.

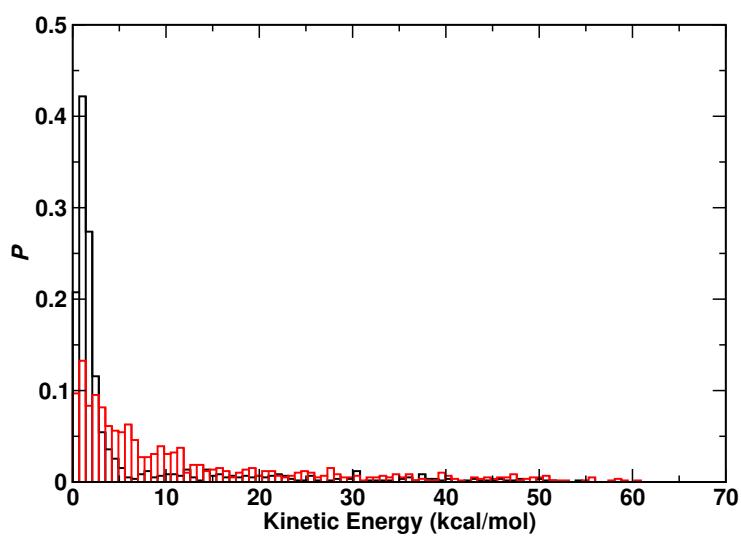


Figure S3: Normalized kinetic energy distribution for CO₂ (red) and NO₂ (black) from 280 reactive trajectories after 450 ps of recombination using RKHS PES. For NO₂ \sim 80 % of trajectories relaxed down to \sim 5 kcal/mol whereas this fraction is only 40 % for CO₂. In other words, upon recombination NO₂ relaxes more effectively than CO₂ on the sub-ns time scale.

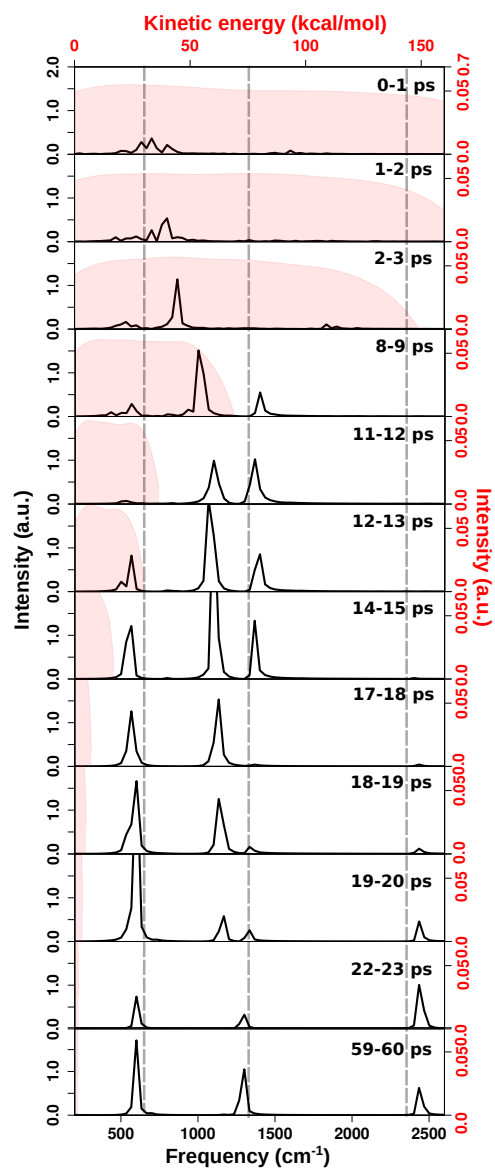


Figure S4: The vibrational density of states power spectrum (black) and kinetic energy distribution (red) of CO₂ after recombination.

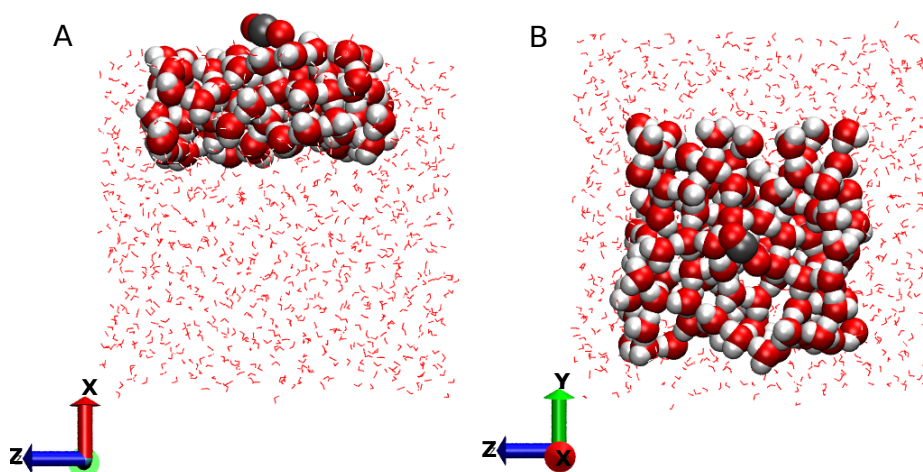


Figure S5: Side (left) and top (right) view of the ASW surface with CO_2 on the top. The water molecules within 10 \AA in the x -direction and 5 \AA in the $y - /z$ -directions are highlighted.

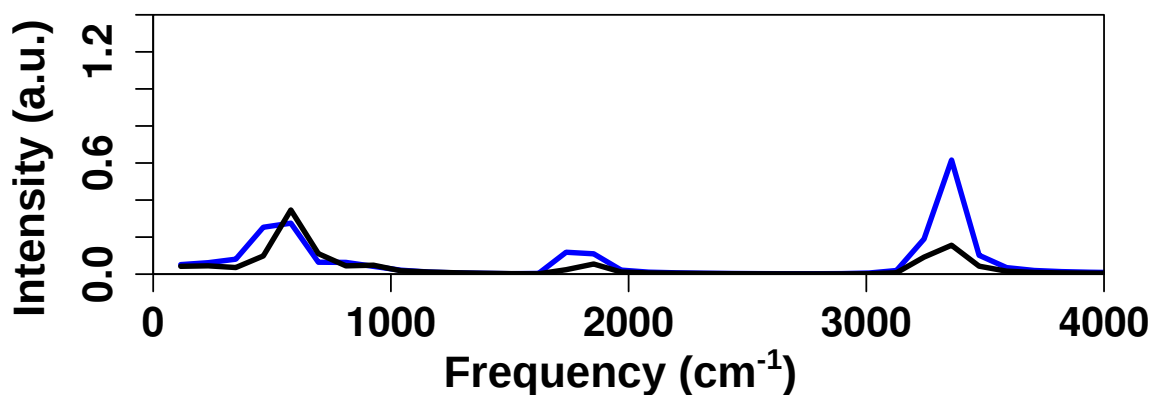


Figure S6: The vDOS spectrum for 10 randomly chosen surface water molecules (including W_A and W_B) before formation of CO_2 (black, thermal equilibrium) and 120 ps after $\text{CO}+\text{O}$ recombination (blue). The spectrum at $t = 120 \text{ ps}$ reproduces all features of the equilibrium vDOS, i.e. the system has returned to equilibrium on the 120 ps time scale. The intensities are “populations of modes within a given frequency interval”.

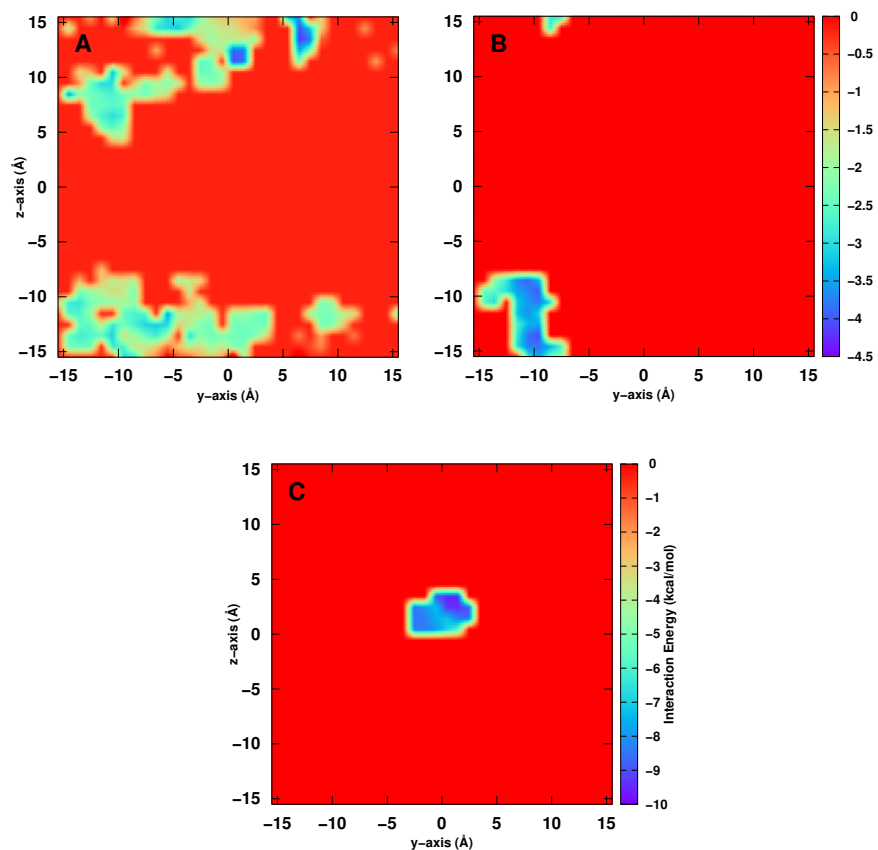


Figure S7: Interaction energy between the respective adsorbate and the ASW projected onto the y/z -plane from a 30 ns long simulation for NO (A), CO₂ (B), and NO₂ (C) on ASW at 50 K. Note that the color codes in panels A and B are the same but differ from that in panel C.

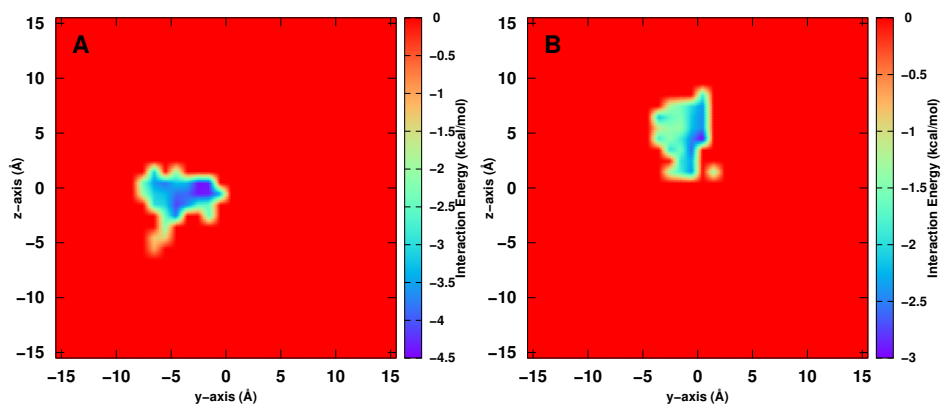


Figure S8: Diffusion of CO₂ (Panel A) and NO₂ (Panel B) on the water surface after recombination ($XO+O \rightarrow XO_2$) was observed in simulations running for 10 ns and 6 ns, respectively. This allows for comparison with the diffusion at 50 K, as shown in Figure S7.